Impedance Characterization of Laser-Induced Graphene (LIG) at X and Ku Band for Low-Profile and Flexible Microwave Structures

Alessio Mostaccio, *Graduate Student Member, IEEE,* Dima Kilani *Senior Member, IEEE,* Gaetano Marrocco, *Senior Member, IEEE,* Mohammad Hossein Zarifi, *Senior Member, IEEE*

***Abstract*—red Laser-Induced Graphene (LIG) is emerging as a sustainable and cost-effective alternative to conventional metallic conductors for microwave applications. However, the understanding of its electrical behavior at high frequencies remains limited.**

This work presents a comprehensive analysis of the surface impedance of LIG traces in the X (8–12 GHz) and Ku (12–18 GHz) frequency bands, by considering three different sets of laser parameters and correlating the measured electrical properties with the morphological features of the conductor.

Results show that, for all the cases considered, the LIG can be modeled as a purely resistive sheet up to 18 GHz, and that the surface resistance remains close to its DC value when beam defocusing is applied. Conversely, for other manufacturing options, such as single and multi-pass scribing, the surface resistance increases by 30–40% due to sample defects.

The extracted impedance is validated both numerically and experimentally using two representative microwave structures: an ultra-wideband monopole antenna (1–18 GHz) and two flexible 4×2 arrays of resonant scatterers working at 9 and 9.5 GHz. In both cases, good agreement is observed between simulation and measurement, with the monopole antenna showing less than 3 dB difference in the realized gain. In the case of the flexible arrays, instead, frequency shifts up to 150 MHz are reported as a result of thermally induced bending of the precursor during laser processing. These findings demonstrate the reliability of the extracted impedance parameters and underscore the importance of incorporating substrate deformation into numerical simulations for more accurate predictions.

***Index Terms*—LIG, Graphene, Characterization, Waveguide, Microwave, Conductivity**

I. Introduction

With the exponential widespread of electronic devices [1] and the growing care for eco-friendly technologies, the replacement of metallic traces in circuits with more sustainable materials is currently paramount. The long-term sustainability of conventional conductors is indeed questioned by the massive environmental efforts required for the extraction and processing of raw materials [2], [3], and the costs related to their disposal [4].

Over the years, various non-metallic conductors have been investigated for microwave applications. PEDOT:PSS stands out among conductive polymers for its film-forming features, tunable conductivity, and transparency, making it suitable for planar resonators [5]–[7]. MXene materials [8], offering excellent microwave performance and processability, have been used to coat 3D-printed components such as waveguides, reducing weight and cost with minimal performance trade-off [9]. Graphene and its derivatives, including carbon nanotubes (CNT) [10]–[12], are attractive for their tunable electrical and mechanical properties. For example, Ju *et al.* demonstrated a stretchable attenuator using CNTs in the ISM band [13]. However, the need for chemical etchants and complex fabrication processes has limited their scalability and eco-compatibility.

In 2014, Li *et al.* discovered a new straightforward technique to synthesize graphene using an infrared (IR) CO_2 laser [14]. The process leverages the photothermal conversion of a carbon-rich precursor, such as polyimide (PI), whose structure is locally rearranged at temperatures exceeding $2500\ ^{\circ}C$, producing a porous, conductive graphene-like trace directly on the substrate.

Beyond its ease of fabrication, Laser-Induced Graphene (LIG) offers key advantages over conventional conductors like copper and silver. It avoids the use of hazardous chemical reagents, and prevents adhesion-related issues, which are critical in flexible and stretchable devices. Moreover, since the conductor is synthesized within the substrate itself, LIG-based devices are inherently lightweight.

Even though LIG has been widely employed to fabricate DC sensors [15]–[18], the possibility of tuning the morphological, electrical, and physical properties of the LIG by simply changing the laser settings, combined with its eco-friendliness, and the low production costs, motivated the use of this material also for the fabrication of antennas [19]–[22], absorbers [23] and resonators [24].

To the best of the authors' knowledge, the effect of the laser settings on LIG's electrical properties has been extensively addressed in DC [25]–[30], and assumed valid also up to a few GHz [31]. Furthermore, no distinction among different manufacturing options producing the same sheet resistance

The work was partly funded by European Union–NextGenerationEU, ECS 0000024 Rome Technopole, CUP B83C22002820006, PNRR Mission 4, Component 2, Investment 1.5. The work was also supported by the Natural Sciences and Engineering Research Council of Canada (NSERC), through grant RGPIN-2018-04288 and the Canadian Foundation for Innovation (CFI) through grant no. 38148 and 37904. The authors would also like to thank CMC Microsystems for their support in the form of software access and equipment. Dr. Alessio Mostaccio and Prof. Gaetano Marrocco are with the Pervasive Electromagnetics Lab, University of Tor Vergata, Rome, 00133, Italy.

Dr. Dima Kilani and Prof. Mohammad H. Zarifi are with Okanagan Microelectronics and Gigahertz Applications (OMEGA) Lab, University of British Columbia Okanagan, Kelowna, V1V 1V7, British Columbia, Canada. The corresponding author is Alessio Mostaccio (e-mail: alessio.mostaccio@uniroma2.it).

Manuscript received April 19, 2021; revised August 16, 2021.

has been made in the above assumption, despite their significantly different impacts on the precursor. Although numerical simulations corroborated the experimental results so far, the surface defects of the trace may introduce a non-negligible effect on the electromagnetic response as the wavelength becomes comparable to their size. In addition, the impact at microwave frequencies of the precursor's thermal deformation, due to the high temperatures involved in the process, has never been either experimentally quantified or considered in simulations. Hence, this paper aims to provide, for the first time, a comprehensive characterization of the LIG in the microwave region by correlating its morphological features with its electrical properties.

In particular, we focused on the X ($8 - 12$ GHz) and Ku ($12 - 18$ GHz) frequency bands, as they facilitate the miniaturization of antennas and microwave components while preserving high efficiency [32], [33]. Moreover, testing within these frequency bands enables the evaluation of electromagnetic interactions with surface defects.

The paper is structured as follows: Section II defines the problem and describes the methods employed for the characterization. Section III introduces the fabrication techniques for the three types of LIG, describes their effects on the substrate, and discusses the morphological features of each sample. Section IV reports the electrical characterization by comparing the extracted values with the DC ones and with other conducting materials. Section V presents the numerical/experimental corroboration using an ultra-wideband monopole antenna and two flexible arrays of scatterers, to validate the estimated electrical properties on a wider frequency range, and evaluate the impact of the precursor surface deformation on the device performance. Finally, Section VI provides the conclusions.

II. Theory & Problem Statement

LIG has been effectively modeled as a thin-film conductor for frequencies up to a few GHz, based on the *thin-film* conductor ($t \leq \delta$) assumption [14], [34], [35]. Due to its reduced thickness, the electromagnetic response of a LIG conductor can be effectively described using Leontovich's boundary condition (1), which relates the tangential components of the electric and magnetic fields through the surface impedance as

$$\boldsymbol{E}_t = Z_s \left(\boldsymbol{H}_t \times \boldsymbol{n} \right) \tag{1}$$

$$Z_S = R_s + jX_s \tag{2}$$

where $\boldsymbol{E}_t$ is the tangential electric field component, Z_s the surface impedance of the LIG conductor, $\boldsymbol{H}_t$ the tangential magnetic field component and $\boldsymbol{n}$ the unit normal vector pointing toward the LIG trace. The surface impedance Z_s can be expressed as in (2) and comprises a real part, namely the surface resistance R_s, representing the resistive (ohmic) losses, and an imaginary part, i.e., the surface reactance X_s, representing the reactive (inductive) behavior of the conductor. The imaginary part is generally negligible in most conventional conductors, but it can become significant in certain materials, such as single- and multi-layer graphene [36]–[38], influencing wave reflection, phase shift, and surface wave propagation.

Under the thin film hypothesis, the surface resistance at relatively low frequency can be replaced by the DC sheet resistance, which can be achieved with simple and low-cost techniques, such as the four-point-probe, or the transfer length methods [39], [40]. However, as the frequency increases, the reduction in penetration depth (δ), along with second-order effects, such as peculiar trace morphologies and thermal bending of the precursor, can cause the surface resistance to deviate from its nominal DC value. Indeed, different settings result in distinct interactions between the laser beam and the precursor, potentially leading to different types of LIG. For example, thermal deformation of the substrate, caused by local overheating during the process, can lead to uneven lasering of the precursor. This occurs due to small local defects, such as wrinkles and depressions, which alter optical parameters, including the focal point. Consequently, the local electrical properties across the surface will not be uniform, causing the resistance values to deviate from the expected ones. Therefore, more accurate estimation methods [37], [38], [41]–[43] are required to reliably measure the conductor's electrical properties.

In this work, we will employ the transmission-line method, as described in [44], and compare the estimated values with the DC measurements. The calculation of Z_s requires an initial calibration phase, during which the scattering parameters, $S_{ij,cal}$, of the PI layer alone are measured. These parameters can be modeled using a π-network, where the series impedance (Z_{sub}) and the shunt admittances ($Y_{s,1} = Y_{s,2} = Y_s$ by symmetry) are determined using (3) and (4).

$$Z_{sub} = Z_0 \frac{(1 + S_{11,cal})^2 - S_{21,cal}^2}{2S_{21,cal}} \tag{3}$$

$$Z_{sub} Y_s^2 + 2Y_s = \frac{(1 + S_{11,cal})^2 - S_{21,cal}^2}{2Z_0 S_{21,cal}} \tag{4}$$

where Z_0 is the characteristic impedance of the waveguide.

Then, by considering the LIG trace as a discontinuity for a wave propagating inside a waveguide, and assuming that the LIG synthesis has a negligible effect on the dielectric properties of the precursors, the surface impedance is calculated using (5)

$$Z_{LIG} = \frac{Z_0 S_{21}}{1 - S_{22} - S_{21} - Z_0 Y_s (1 + S_{22} + S_{21})} \tag{5}$$

where S_{ij} are the S-parameters measured upon the engraving of the LIG trace on the precursor.

III. Samples Characterization

A. Synthesis & Morphological Characterization of LIG

We will focus on three types of LIG obtained with three well-established manufacturing options for the synthesis of a high-quality LIG, as illustrated in Fig. 1. They are denoted as

1) LIG-S or single-pass, which resorts to a high-power focused beam to obtain high conductivity values [45];
2) LIG-MP or multi-pass, which scribes the same area multiple times [46];

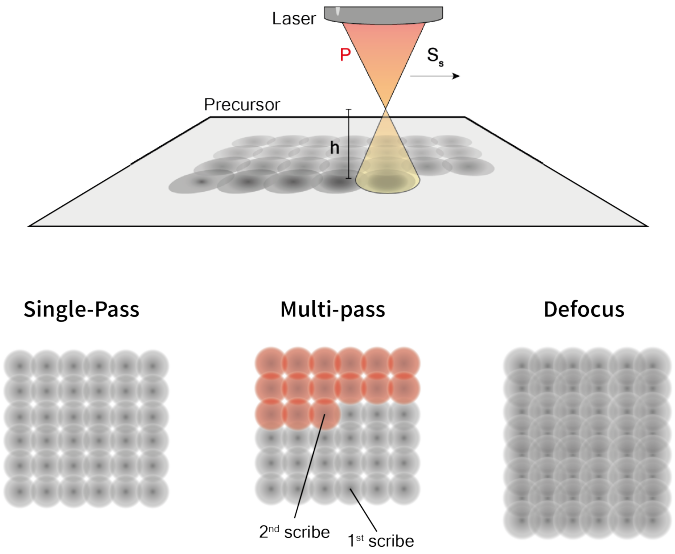

Fig. 1: Schematic representation of laser settings and fabrication process for LIG-S, LIG-MP, and LIG-D.

TABLE I
LASER SETTINGS FOR EACH LIG SPECIMEN

Type	P (W)	S_s $\left(\frac{cm}{s}\right)$	N (−)	h (mm)	F $\left(\frac{J}{cm^2}\right)$
LIG-S	8.8	14.4	1	0	14.6
LIG-MP	8.8	14.4	2	0	14.6
LIG-D	8.8	14.4	1	3	7.8

3) LIG-D or defocused, which introduces a vertical offset, h, between the focal point and the surface of the precursor [46].

Although the single-pass and multi-pass processes share the same spot size, and, in turn, the same laser fluence (i..e, the optical energy delivered per pulse per unit area [47]), the multi-pass approach overall delivers a higher amount of energy, by distributing it across distinct time intervals. Accordingly, a larger amount of the precursor can be converted into LIG without ablation. In contrast, the defocusing widens the spot size, thus introducing a twofold effect: *(i)* reduction in the laser fluence, and *(ii)* an increased overlapping between adjacent spots that, in turn, corresponds to an higher homogeneity of the conductor [34], [46]–[48].

All the LIG samples considered hereafter were synthesized from commercially available polyimide (PI) films (McMaster-Carr, Kapton Polyimide film, 125 μm thick) using an infrared (IR) CO_2 laser cutter (Glowforge Plus). Prior to sample fabrication, a hardware-specific calibration phase was performed to fine-tune the laser settings for optimal LIG synthesis [31]. Table I summarizes the fabrication parameters including the estimated laser fluence[1] for each configuration. The *single-pass* sample was fabricated by slightly adjusting the values of laser power P and scan speed S_s as in [40]. The other

[1]Assuming a Gaussian beam profile with a spot diameter of 100 μm (focused) and 200 μm (defocused), the laser fluence is computed as $F = E/A$, where $E = P/(PPI \cdot S)$ is the energy, $PPI = 1355$ is the pulse-per-inch parameter, and A is the corresponding spot area.

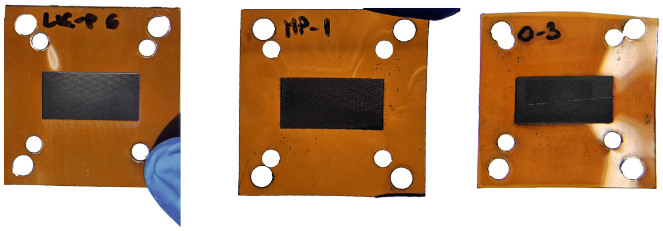

(a) (b) (c)

Fig. 2: Fabricated samples of (a) LIG-S, (b) LIG-MP, and (c) LIG-D employed for the characterization

TABLE II
MORPHOLOGICAL FEATURES OF EACH LIG SAMPLE

	LIG-S	LIG-MP	LIG-D
I_D/I_G (−)	0.80 ± 0.04	0.60 ± 0.12	0.49 ± 0.27
I_{2D}/I_G (−)	0.71 ± 0.03	0.68 ± 0.00	0.81 ± 0.13
t_{up} (μm)	18.6 ± 5.5	6.1 ± 6.0	29.8 ± 3.2
t_{down} (μm)	34.0 ± 11.1	41.4 ± 5.9	24.4 ± 2.6
t (μm)	52.6 ± 12.4	47.5 ± 8.4	54.2 ± 4.1
a_x ($\mu m/mm$)	7.44	6.45	3.55
a_y (m/mm)	−9.41	−10.8	−6.75

two samples, instead, namely LIG-MP (multi-pass) and LIG-D (defocus), were achieved by considering a higher number of passes ($N = 2$) and a vertical offset ($h = 3$ mm) in addition to the previous settings.

The morphological characterization of the traces was conducted on specimens measuring 23 $mm \times 11$ mm, matching the widest aperture of the waveguides studied (Fig. 2). This size minimizes parasitic capacitive effects from the flanges [44], improving the accuracy of surface reactance estimation while maintaining a reliable electrical connection.

The comparison on the macroscopic scale highlights that LIG-MP has the darkest appearance, whereas LIG-D trace shows the greatest compactness.

SEM images of the three samples are presented in Fig. 3a-3c. As expected, the LIG-S sample (Fig. 3a) exhibits more porosity than the LIG-MP one (Fig. 3b), which has a compact and uniform structure due to the higher amount of precursor converted. In contrast, LIG-D exhibits a uniform morphology despite the presence of larger pores (Fig. 3c). This outcome arises from beam defocusing, which introduces two competing effects. First, the laser spot widens, reducing the energy density delivered per pulse to the precursor. Second, the overlap between adjacent spots increases [49]. These combined effects result in a more compact trace, where heat and gases are released through surface blisters. Upon rupturing, these blisters are replaced by pores [47].

The Raman spectra of the fabricated LIG samples are reported in Fig. 3d-3f. The quality of the generated graphene can be evaluated by the inspection of the I_D, I_G, and I_{2D} peaks, whose positions and shapes indicate the amount of defects, the presence of sp_2-hybridized carbon network, and the number of layers, respectively [40], [45], [50]. As reported

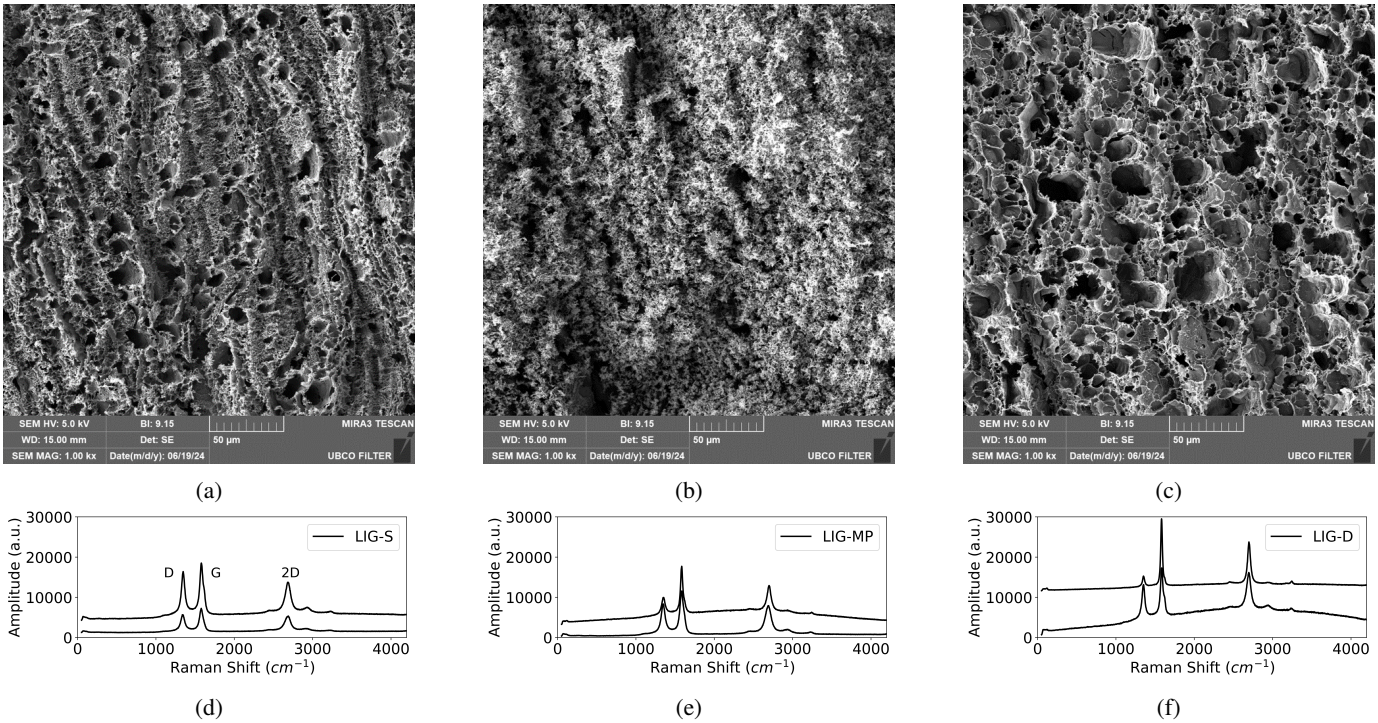

Fig. 3: (a)-(c) Scanning Electron Microscope (SEM) images (Mira 3 by TESCAN, with $HV = 15$ kV, Mag=1000X, and $WD = 15$ mm) with the corresponding settings, (d)-(f) Raman spectra (SENTERRA II confocal Raman microscope) of two different specimens for the three samples of LIG.

in Table II, LIG-S exhibits a I_D/I_G ratio close to 1, compared to LIG-D, which, instead, shows the lowest I_D/I_G ratio and thus the lowest defectivity[2]. Additionally, the comparison of the I_{2D}/I_G ratio suggests that the number of graphene layers decreases with the introduction of defocusing, indicating a transition toward a single-layer graphene structure.[3]

B. Thickness

LIG formation occurs both within the cross-section of the precursor and above its surface as a consequence of its synthesis process. Accordingly, the overall thickness of the trace is the summation of two distinct contributions (6) as shown in Fig. 4.

$$t = t_{down} + t_{up} \tag{6}$$

The upward step, t_{up}, is the discontinuity from the precursor to the upper surface of LIG, whereas t_{down} is the step from the unlasered precursor to the lasered one, or engraving depth. Both contributions are measured by a laser profilometer (Olympus LEXT OSL5000 Laser Confocal Microscope, 20x Magnification) with the latter being evaluated upon the removal of the LIG trace from the polymer. To effectively remove LIG without damaging the precursor, the engraved PI sample was previously pasted on a rigid substrate by means of double-sided tape and then peeled off. As a matter of fact, the LIG particles can be indirectly removed from the precursor when an abrupt mechanical stimulus, such as the rapid peeling

[2]The lower the I_D/I_G ratio, the lower the amount of defects.

[3]The closer the I_{2D}/I_G ratio to 1, the closer the graphene to a single-layer structure.

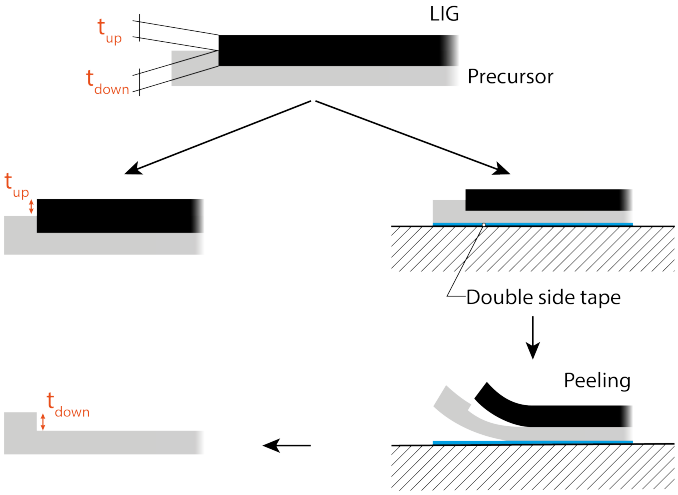

Fig. 4: Sketch of the tape method employed to estimate the thickness of the LIG.

of the PI from the rigid substrate, is applied. This avoids the need for a direct removal (e.g., with a knife) that, in turn, would introduce measurement artifacts.

Table II resumes the measured thicknesses. All the samples have an average value of approximately $50\ \mu m$ and an inter-sample variability decreasing from $\pm 20\%$ for LIG-S down to $\pm 8\%$ for LIG-D. Using LIG-S as the reference for comparison and considering the values of t_{up} and t_{down}, LIG-MP shows the deepest engraving into the precursor material and the shallowest upward step as a consequence of the multiple scribing. In contrast, LIG-D exhibits a more even distribution of the

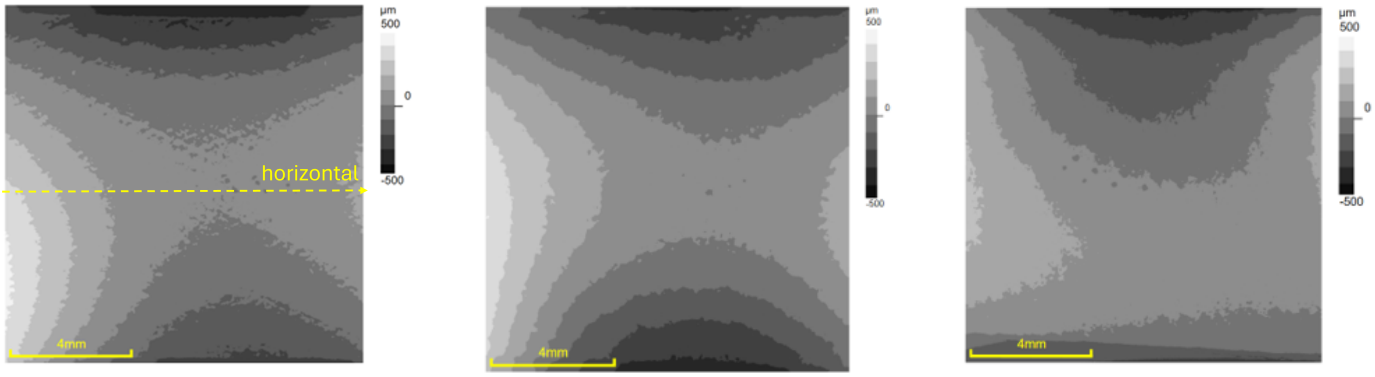

(a) (b) (c)

Fig. 5: Surface profile as a consequence of the thermal bending for (a) LIG-S, (b) LIG-MP, and (c) LIG-D.

conductor across the substrate, which is due to the more gentle engraving, reducing t_{down}, but also to the aforementioned blistering of the PI surface, which, in turn, increases t_{up}. The above results are in agreement with [14], [34], [35], [51], [52].

C. Thermal Bending

The deformations of the LIG-S, LIG-MP, and LIG-D traces caused by thermal stress during fabrication were measured by means of the laser profilometer (5x magnification) with the magnifications of the central portions (12mm x 12 mm) being reported in Fig. 5a-5c.

All samples display a hyperbolic paraboloid bending pattern, with expansion along the lasering direction and contraction perpendicularly to that. The bending fitting coefficients from (7), a_x and a_y, for the three samples are compared in Table II.

To correlate the fabrication methods to the deformation of precursor, the surface profile of the trace $P(x, y)$ was parametrized by means of a quadratic curve (7) and the coefficients $\{a_X,\ a_Y\}$ were considered as the bending features.

$$P(x, y) = a_X x^2 + a_Y y^2 \tag{7}$$

These were estimated experimentally by fitting the deformation of each LIG sample, along the x and y directions, with the quadratic polynomial in (7).

Defocusing the beam is the less aggressive approach, as it significantly reduces precursor deformation in both directions compared to LIG-S. In contrast, for LIG-MP specimens, performing a second pass over the same area helps average out thermally induced defects, such as wrinkles and depressions, thereby mitigating their effects, even though the overall deformation remains unchanged.

The analysis suggested that the thermal bending *(i)* is correlated with the engraving depth, since smaller values of t_{down} correspond to lower deformations, and *(ii)* it is a local phenomenon governed by the energy of each spot rather than by the total energy delivered across the area. Each pulse, indeed, locally introduces stress into the substrate proportionally to the energy delivered; accordingly, the enlargement of the beam cross-section due to the vertical offset reduces the local energy density by spreading the same amount of power over a wider area. In contrast, the additional energy provided by higher overlapping (for LIG-D) and multiple scribing (for LIG-MP) is delivered to the surface after the initial pulse, rather than simultaneously, thus providing a second-order contribution to the local deformation.

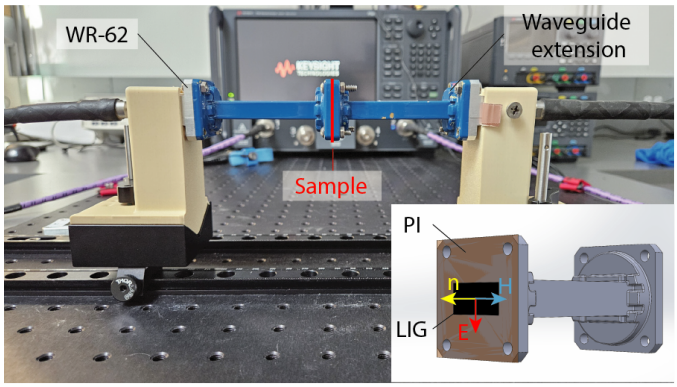

Fig. 6: Measurement setup for the characterization of LIG in the Ku-band. Isometric sketch of the setup along with the direction of the vectors $\boldsymbol{E}$, $\boldsymbol{H}$, and $\boldsymbol{n}$ w.r.t. the LIG sample in the inset.

D. DC Sheet Resistance

The DC Sheet resistance was evaluated by the *four-point-probe* method [39] by means of the ResTest Test Unit by Jandel. A correction factor $C_f = 0.93$ was applied to account for the rectangular geometry of the sample and the instrument's probe spacing ($s = 1.27\ mm$).

IV. LIG CHARACTERIZATION AT MICROWAVE FREQUENCIES

The experimental setup for the microwave characterization is reported in Fig. 6, along with the orientation of the tangential electric and magnetic fields. To cover both the X and Ku bands, two types of waveguides and their extensions were employed, namely the WR-90 from 8 to 12.4 GHz and the WR-62 from 12 to 18 GHz.

The waveguides were placed on a quasi-optical table by means of 3D-printed supports and connected to the Vector Network Analyzer (Keysight PNA N5222b). The alignment

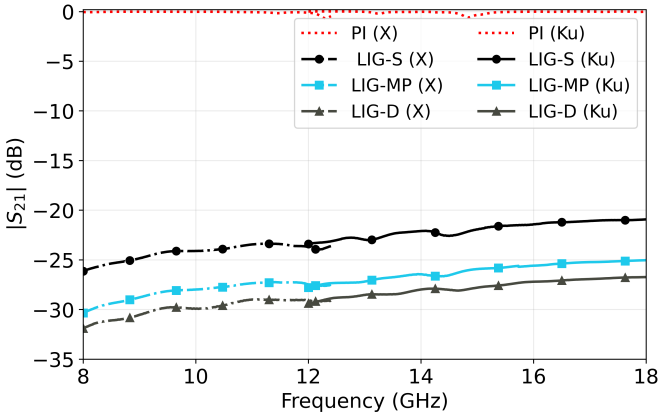

(a)

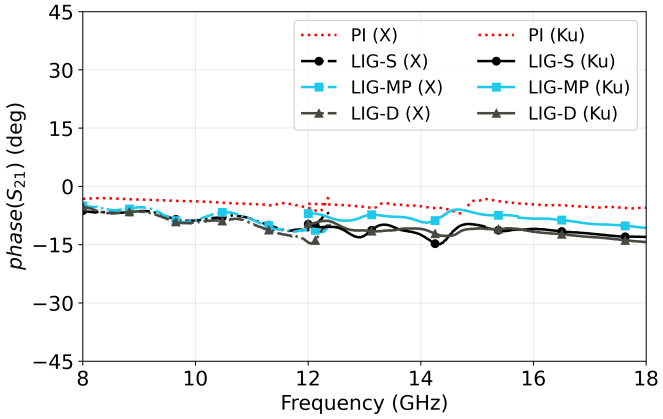

(b)

Fig. 7: Average measured (a) module and (b) phase of S_{21} for LIG-S (circle), LIG-MP (square), and LIG-D (triangle) in the X (solid) and Ku (dot-dash) bands. Red dotted line for the bare PI layer.

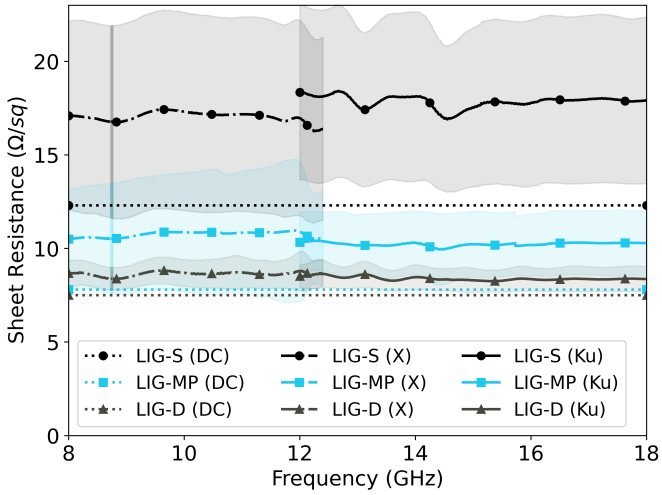

Fig. 8: Average extracted surface resistance and the corresponding standard deviation (shaded area). The dotted line represents the average value in DC.

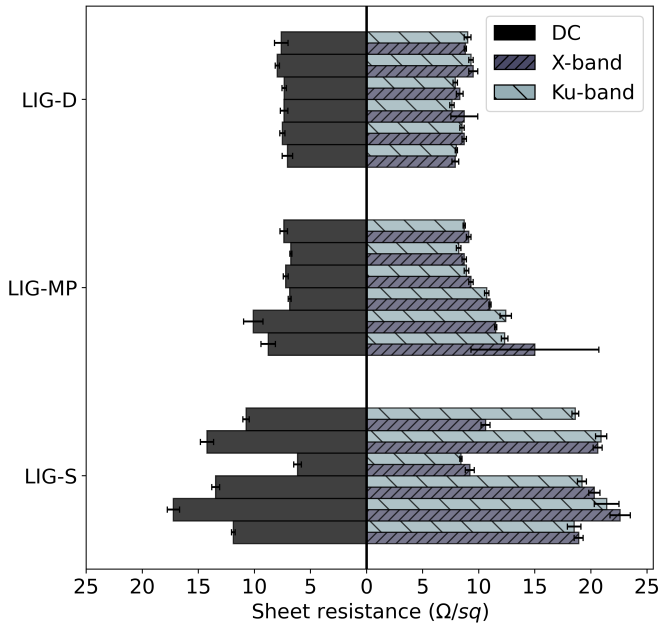

Fig. 9: Average measured sheet resistance in DC (left) and in the X, Ku bands (right) with the corresponding standard deviation for the 6 samples of LIG-S, LIG-MP, and LIG-D.

holes on the waveguide flanges were replicated on the PI film to align the samples to the apertures by means of metallic screws. The latter were tightened to reduce air gaps, and the measurement was repeated 10 times for each specimen to assess the repeatability. The size of the LIG trace is marginally larger than that of the WR-90 waveguide aperture, the widest among the considered apertures, to minimize the capacitive effect between the edge of the sample and that of the waveguide [44].

The module and the phase of the measured transmission coefficient S_{21} of the waveguide system in the X and Ku bands, with the LIG-S, LIG-MP, and LIG-D samples placed in between are shown in Fig. 7a and 7b. The $|S_{21}|$ level for different samples is between -35 dB and -20 dB, mainly due to the different levels of penetration and partial attenuation of the impinging fields crossing the LIG discontinuity. For the PI layer, the average amplitude is zero, as expected. Regarding the phase response, no significant phase shift is introduced by the LIG samples, and no difference is evident when compared to the bare PI layer. Accordingly, no reactive contribution in the surface impedance is expected by the LIG. Fig. 8 shows the estimated average sheet resistance w.r.t. frequency, along with the variability among samples of the same type. The results clearly indicate a frequency-independent behavior of the LIG in the two bands of interest. Fig. 9 and Table III, instead, provide a comparison between the DC and microwave (both X and Ku bands) values of sheet resistance for each sample.

Notably, as the frequency increases from DC to higher ranges, LIG-S maintains the highest sheet resistance, despite an average increase of 40% and considerable inter-sample variability. This behavior is likely due to significant thermal bending of the precursor, which unpredictably alters local lasering conditions. LIG-MP shows at least a 30% increase in sheet resistance, but, the second scribing process results in a more compact trace structure, and, in turn, reduced variability across samples. In both cases, this deterioration will cause a

TABLE III
AVERAGE MEASURED SHEET RESISTANCE (Ω/sq)

	LIG-S	LIG-MP	LIG-D
DC	12.3 ± 3.4	7.8 ± 1.3	7.5 ± 0.5
X-band	17.0 ± 5.2	10.7 ± 3.1	8.6 ± 0.7
Ku-band	17.9 ± 4.4	10.2 ± 1.7	8.4 ± 0.6

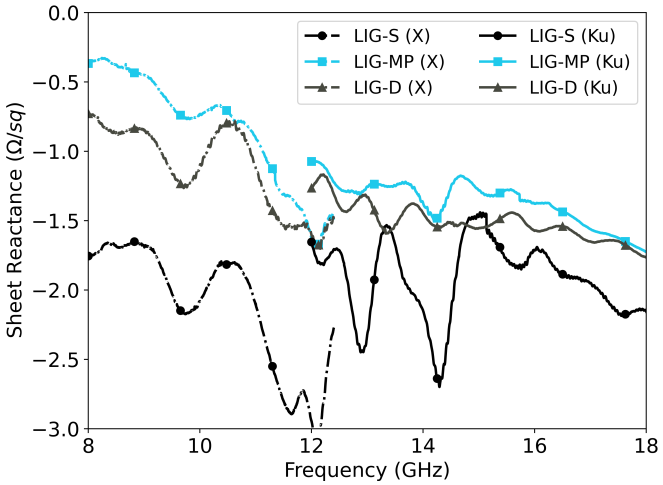

Fig. 10: Extracted surface reactance in the X (solid) and Ku (dot-dash) bands for LIG-S (circle), LIG-MP (square) and LIG-D (triangle).

10% decrease of the maximum achievable radiation efficiency for a $\lambda/2$ dipole, as demonstrated in [31]. In contrast, LIG-D undergoes a much more contained deterioration of performance ($\approx 13\%$).

The same method was then employed to extract the surface reactance values (X_s) presented in Fig. 10. For all the samples, a small negative contribution, i.e., capacitive, is estimated, although the latter can be considered an artifact introduced by the parasitic capacitance formed between the two waveguides, as demonstrated in [44]. Therefore, the reactive component of the surface impedance of LIG is negligible for frequencies up to 18 GHz regardless of the laser settings.

Finally, Table IV summarizes the value of sheet resistance and electrical conductivity for the LIG and compares the latter with other conventional conductors.

A. Frequency Range of applicability

Under the thin-film conductor assumption ($t \leq \delta$), the conductivity of the LIG traces can be computed as in (8)

$$\sigma = \frac{1}{R_s t} \tag{8}$$

By substituting (8) into the expression for the penetration depth (9), and setting $t = \delta$, the maximum frequency, f_{lim}, up to which the presented results remain valid, can be determined as in (10):

$$\delta = \sqrt{\frac{1}{\pi f \mu_0 \sigma}} = \sqrt{\frac{R_s t}{\pi f \mu_0}} \tag{9}$$

TABLE IV
COMPARISON OF THE SHEET RESISTANCE AND CONDUCTIVITY VALUES FOR THE LIG AND OTHER CONDUCTORS @ 10 GHZ (U: UNDOPED, D: DOPED)

	$\mathbf{R_s}$ ($\mathbf{\Omega/sq}$)	σ ($\mathbf{S/cm}$)	**Ref.**
LIG-S	17.0	11.2	This work
LIG-MP	10.7	19.7	This work
LIG-D	8.6	21.1	This work
Copper	$4.0 \cdot 10^{-4}$	$5.6 \cdot 10^{5}$	-
Ag ink	$5.0 \cdot 10^{-2}$	$8.3 \cdot 10^{3}$	[53]
PEDOT:PSS (U)	$1.0 \cdot 10^{4}$	1	[5]
PEDOT:PSS (D)	4.0	$1.2 \cdot 10^{3}$	[54]
CNT (U)	100.0	50	[55]
CNT (D)	1.3	$3.7 \cdot 10^{3}$	[56]
MXene	0.8	$12.5 \cdot 10^{3}$	[9]

$$f_{lim} = \frac{R_s}{\pi \mu_0 t} \tag{10}$$

Therefore, by considering the lowest sheet resistance, i.e., that of LIG-D, an upper-bound frequency $f_{lim} \approx 40\ GHz$ can be calculated

V. NUMERICAL/EXPERIMENTAL CORROBORATION

Finally, this Section aims to validate the achieved experimental results by considering two examples of typical microwave devices. The first one is a rigid ultra-wideband (UWB) monopole antenna to corroborate the estimated electrical properties on a wider frequency range. The second scenario involves two arrays of square scatterers resonating at distinct frequencies. Without any loss of generality, both prototypes are referred to LIG-D settings only.

The LIG was modeled on Ansys HFSS through the Impedance Boundary Condition by considering the conductor as electromagnetically penetrable and by enforcing Leontovich's Condition on its surface as in (1), where $Z_s \approx R_s$ [57]. Specifically, the value of surface resistance considered is the average value calculated in the band of interest.

A. Ultra-wideband monopole antenna

The UWB disk monopole layout is adapted from the literature [58], with minor geometric modifications for impedance matching. For each type of LIG, two identical antennas, spaced 30 cm apart, were simulated from 1 to 18 GHz to retrieve the full S-matrix.

Then, each sample was fabricated: preliminarily, to preserve the mechanical rigidity during the engraving, the PI film precursor was attached on a Poly-methyl-methacrylate (PMMA) layer (0.8 mm thick) by means of double-sided tape, and its surface was cleaned with distilled water. Hence, the antenna was engraved by resorting to LIG-D settings (Table I), and the high-precision 2.4 mm SMA connector was attached to the LIG trace by means of the CW2400 conductive epoxy by Chemtronics [59].

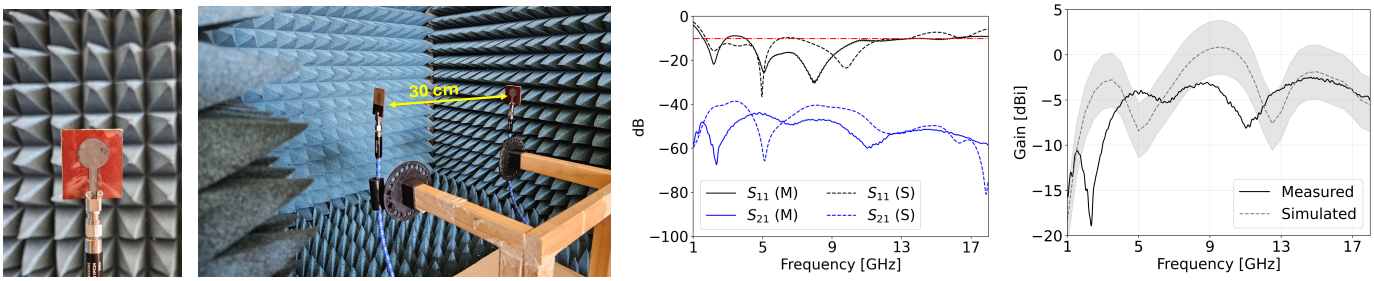

(a) (b) (c) (d)

Fig. 11: Photo of (a) the manufactured UWB monopole antenna, and (b) the two-ports setup for its characterization. (c) Comparison between measured (solid) and simulated (dashed) S_{11} (black) and S_{21} (blue) curves for the UWB monopole antenna. (d) Estimated (solid) and simulated (dashed) realized gain. ± 3 dB uncertainty due to manufacturing imperfections in the shaded area.

Fig. 11a and 11b show the fabricated prototype along with the two-port setup employed for the characterization of the antennas, in a semi-anechoic environment. Fig. 11c shows the measured and simulated S-parameters averaged over the two prototypes. Despite visible frequency shifts, which are more pronounced at lower frequencies due to ambient reflections, the overall agreement with simulation remains satisfactory.

Based on the S-matrix measurements, the realized gain of the antenna was computed by means of the Friis formula, and by assuming identical the two prototypes [60]

As shown in Fig. 11d, aside from the aforementioned frequency shift, the measured and simulated gain values differ by no more than 3 dB, likely due to losses at the connector–LIG interface. This confirms the accuracy of the extracted surface impedance and validates its use in modeling LIG-based microwave devices.

B. Flexible array of scatterers

To quantify how much the simulations are sensitive to the thermal bending of the manufactured samples, two flexible 4×2 arrays of square scatterers, named hereafter A_1 and A_2, resonating at two different frequencies (layout and size in Fig. 12a) were simulated and tested in the X-band, and by using PI film only as a precursor.

Fig. 12b presents the measurement setup with the two fabricated arrays attached on a styrofoam block for mechanical support and placed in front of an open-ended WR-90 waveguide at a distance $d = 20$ mm by means of a 3D-printed holder. The reflection coefficient S_{11} of the antenna was measured by considering orthogonal incidence only.

Fig. 13 compares the measured and simulated responses for both arrays. Two simulation scenarios are presented: first, assuming no thermal bending (dotted curve), where the arrays are modeled as fully planar; second, incorporating the deformation observed in Section III-C. In this case, each LIG patch is bent according to Equation (7) and Table II for LIG-D, resulting in a curved configuration (dashed line).

Notably, the deformation of the precursor has a significant impact by producing a frequency shift up to 150 MHz despite the latter being non-monotonic. The results show a good agreement between the curves, apart from a small frequency shift due to the approximate manual positioning of the array in front of the waveguide.

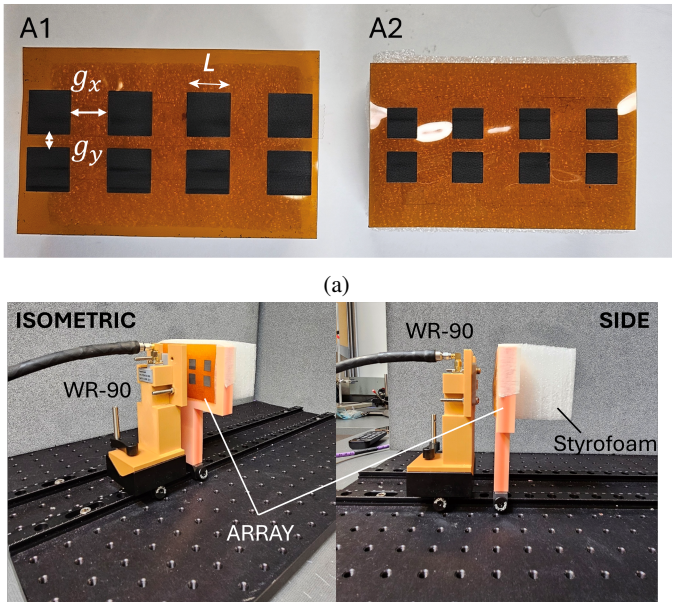

(a)

(b)

Fig. 12: (a) Manufactured scatterers. [A_1: $L = 16$ mm, $g_x = 14$ mm, $g_y = 5$ mm], [A_2: $L = 11$ mm, $g_x = 13$ mm, $g_y = 5$ mm]. (b) Isometric and side views of the experimental setup employed for measurements.

However, when analyzing the frequency shift caused by thermal bending across different L/g_x ratios (Fig. 14a), it becomes evident that this effect is more detrimental for smaller patches spaced farther apart, even though the trend is not strictly monotonic

The impact of the approximate knowledge of the surface resistance on the electromagnetic response was evaluated by simulations in Fig. 14b. For the A_2 layout, indeed, the R_s of the patches varied between 5 Ω/sq and 15 Ω/sq, and the resonance frequency and the amplitude of the reflection coefficient were extracted. Notably, the latter is the most sensitive parameter to the variation of surface resistance, although no significant difference is observed when the DC sheet resistance is considered instead of R_s. In contrast, the resonance frequency is minimally affected even for large variations of R_s.

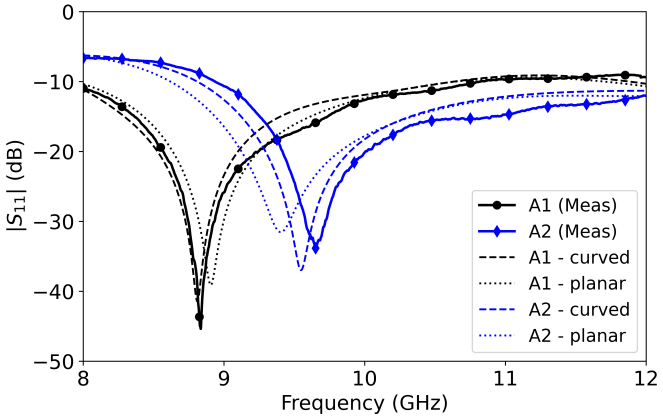

Fig. 13: Measured (solid) and simulated reflection coefficient of the WR-90 waveguide when the A_1 (black) and A_2 (blue) array is placed at a distance $d = 20\ mm$. Simulations include both the planar (dashed) and curved (dotted) configurations of the array.

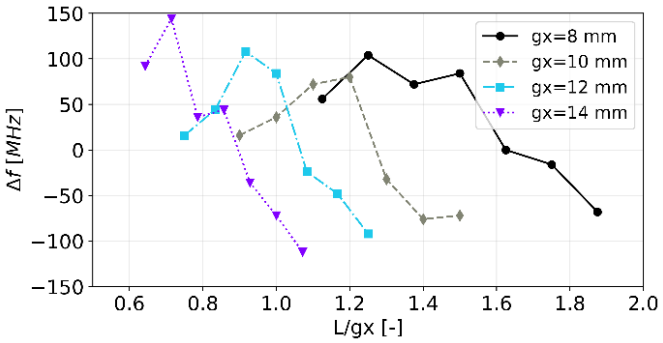

(a)

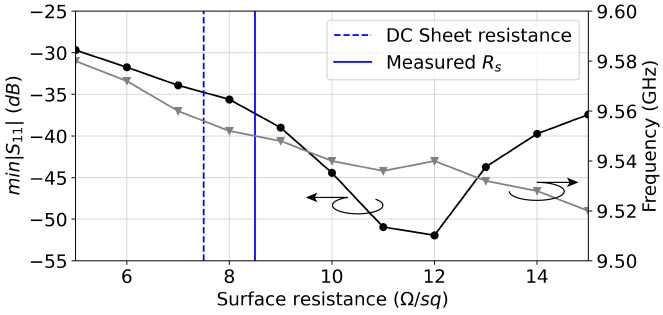

(b)

Fig. 14: (a) Frequency shift due to thermal bending of A_1 for different L/g_x ratios. (b) Impact of the sheet resistance on the minimum of the reflection coefficient (left) and resonance frequency (right).

VI. Conclusion

The paper has presented an experimental characterization, in the X and Ku frequency bands, of the electrical properties of the LIG on PI, obtained with three different manufacturing options. The results have been correlated with the morphological features of the samples and then corroborated with simulations.

The findings suggest that, despite providing the same improvement in sheet resistance as in DC, multi-pass and defocus techniques affect microwave electrical properties differently. For LIG-D, the variation of surface resistance with frequency relative to DC is almost negligible, making the DC sheet resistance a reliable approximation with the advantage of a simpler measurement process. In contrast, the other fabrication methods exhibit surface resistance at least 30% higher than the DC value.

The intrinsic reactive contribution of the material was found to be negligible in the band of interest for all three manufacturing options. This is probably due to the high defectiveness of the LIG, which decreases the kinetic inductance of the material. Therefore, up to 18 GHz, LIG can be accurately modeled as a pure resistive load.

Experimental validation using a UWB monopole antenna confirmed the accuracy of surface impedance estimation, with measured antenna performances aligning with simulations. Additionally, tests on thin scatterer arrays highlighted the significant impact of thermal bending on resonance frequency, underscoring the importance of accounting for substrate deformation in numerical simulations for precise tuning.

In conclusion, our findings provide valuable insights for microwave designers, emphasizing how fabrication-related characteristics of the conductor can influence the performance of LIG-based devices.

Acknowledgments

The authors recognize and express their gratitude to the Syilx Okanagan Nation for the use of their unceded territory, the land on which this research was conducted. The authors wish to thank the Fipke Laboratory for Trace Element Research (FiLTER) at UBCO for the use of their facilities.

References

[1] F. Brügge, M. Hasan, M. Kulezak, K. L. Lueth, E. Pasqua, S. Sinha, P. Wegner, K. Baviskar, and A. Taparia, *State of IoT – Spring 2023*.

[2] R. Arendt, V. Bach, and M. Finkbeiner, "The global environmental costs of mining and processing abiotic raw materials and their geographic distribution," *Journal of Cleaner Production*, vol. 361, p. 132232, 2022.

[3] J. Spooren, K. Binnemans, J. Björkmalm, K. Breemersch, Y. Dams, K. Folens, M. González-Moya, L. Horckmans, K. Komnitsas, W. Kurylak *et al.*, "Near-zero-waste processing of low-grade, complex primary ores and secondary raw materials in europe: technology development trends," *Resources, Conservation and Recycling*, vol. 160, p. 104919, 2020.

[4] C. P. Baldé, R. Kuehr, T. Yamamoto, R. McDonald, E. D'Angelo, S. Althaf, G. Bel, O. Deubzer, E. Fernandez-Cubillo, V. Forti, S. Gray, Vanessa Herat, S. Honda, G. Iattoni, D. S. Khetriwal, V. Luda di Cortemiglia, Y. Lobuntsova, I. Nnorom, N. Pralat, and M. Wagner, *The Global E-Waste Monitor 2024*.

[5] H. Shi, C. Liu, Q. Jiang, and J. Xu, "Effective approaches to improve the electrical conductivity of pedot: Pss: a review," *Advanced Electronic Materials*, vol. 1, no. 4, p. 1500017, 2015.

[6] L. V. Kayser and D. J. Lipomi, "Stretchable conductive polymers and composites based on pedot and pedot: Pss," *Advanced Materials*, vol. 31, no. 10, p. 1806133, 2019.

[7] M. Moradpour and M. H. Zarifi, "High-resolution pedot: Pss-based planar microwave resonator sensor," *IEEE Sensors Journal*, vol. 23, no. 18, pp. 21 216–21 225, 2023.

[8] O. Niksan, B. C. Wyatt, K. K. Kazemi, B. Anasori, and M. H. Zarifi, "Mxene free standing films: unlocking the impact of flake sizes in microwave resonant structures in humid environments," *Small*, vol. 19, no. 37, p. 2300848, 2023.

[9] O. Niksan, L. Bi, K. K. Kazemi, R. Rakhmanov, Y. Gogotsi, and M. H. Zarifi, "Mxene guides microwaves through 3d polymeric structures," *Materials Today*, vol. 73, pp. 47–55, 2024.

[10] C. Soldano, A. Mahmood, and E. Dujardin, "Production, properties and potential of graphene," *Carbon*, vol. 48, no. 8, pp. 2127–2150, 2010.

[11] N. Mohd Nurazzi, M. M. Asyraf, A. Khalina, N. Abdullah, F. A. Sabaruddin, S. H. Kamarudin, S. Ahmad, A. M. Mahat, C. L. Lee, H. Aisyah *et al.*, "Fabrication, functionalization, and application of carbon nanotube-reinforced polymer composite: An overview," *Polymers*, vol. 13, no. 7, p. 1047, 2021.

[12] K. R. G. Lim, M. Shekhirev, B. C. Wyatt, B. Anasori, Y. Gogotsi, and Z. W. Seh, "Fundamentals of mxene synthesis," *Nature Synthesis*, vol. 1, no. 8, pp. 601–614, 2022.

[13] L. Ju, Z.-G. Liu, B.-Y. Yu, H. Chen, Z.-D. Xiao, and W.-B. Lu, "Stretchable and dynamically tunable attenuator based on graphene," *IEEE Transactions on Microwave Theory and Techniques*, vol. 70, no. 6, pp. 2999–3008, 2022.

[14] R. Ye, D. K. James, and J. M. Tour, "Laser-induced graphene: from discovery to translation," *Advanced Materials*, vol. 31, no. 1, p. 1803621, 2019.

[15] M. G. Stanford, K. Yang, Y. Chyan, C. Kittrell, and J. M. Tour, "Laser-induced graphene for flexible and embeddable gas sensors," *ACS nano*, vol. 13, no. 3, pp. 3474–3482, 2019.

[16] F. M. Vivaldi, A. Dallinger, A. Bonini, N. Poma, L. Sembranti, D. Biagini, P. Salvo, F. Greco, and F. Di Francesco, "Three-dimensional (3d) laser-induced graphene: Structure, properties, and application to chemical sensing," *ACS Applied Materials & Interfaces*, vol. 13, no. 26, pp. 30 245–30 260, 2021.

[17] L. Huang, J. Su, Y. Song, and R. Ye, "Laser-induced graphene: En route to smart sensing," *Nano-micro letters*, vol. 12, pp. 1–17, 2020.

[18] B. Kulyk, B. F. Silva, A. F. Carvalho, S. Silvestre, A. J. Fernandes, R. Martins, E. Fortunato, and F. M. Costa, "Laser-induced graphene from paper for mechanical sensing," *ACS Applied Materials & Interfaces*, vol. 13, no. 8, pp. 10 210–10 221, 2021.

[19] F. P. Chietera, R. Colella, A. Verma, E. Ferraris, C. E. Corcione, C. L. Moraila-Martinez, D. Gerardo, Y. H. Acid, A. Rivadeneyra, and L. Catarinucci, "Laser-induced graphene, fused filament fabrication, and aerosol jet printing for realizing conductive elements of uhf rfid antennas," *IEEE Journal of Radio Frequency Identification*, vol. 6, pp. 601–609, 2022.

[20] A. Mostaccio, F. Naccarata, F. M. C. Nanni, J. Filippi, E. Martinelli, and G. Marrocco, "Soft and flexible wireless epidermal plaster made by laser-induced graphene," *IEEE Sensors Letters*, 2024.

[21] A. Mostaccio, G. Antonelli, R. Capuano, C. Di Natale, E. Martinelli, and G. Marrocco, "Full-lig wireless battery-less flexible sensor for the detection of triethylamine," *IEEE Journal on Flexible Electronics*, 2024.

[22] M. Ahmad, G. Cantarella, M. A. C. Angeli, M. Madagalam, C. Ebner, M. Ciocca, R. Riaz, P. Ibba, M. Petrelli, I. Merino *et al.*, "2.4 ghz microstrip patch antenna fabricated by means of laser induced graphitization of a cellulose-based paper substrate," in *2021 IEEE International Flexible Electronics Technology Conference (IFETC)*. IEEE, 2021, pp. 0044–0046.

[23] Y. Houeix, F. J. Romero, F. G. Ruiz, D. P. Morales, N. Rodriguez, and D. Kaddour, "Thin microwave absorber based on laser-induced graphene frequency selective surfaces," *IEEE Journal of Radio Frequency Identification*, 2024.

[24] W. Yuan, S. Liu, and X. Zhang, "A flexible chipless rfid strain sensor with high sensitivity based on laser-induced graphene," *Sensors and Actuators A: Physical*, vol. 382, p. 116144, 2025.

[25] Y. Li, D. X. Luong, J. Zhang, Y. R. Tarkunde, C. Kittrell, F. Sargunaraj, Y. Ji, C. J. Arnusch, and J. M. Tour, "Laser-induced graphene in controlled atmospheres: from superhydrophilic to superhydrophobic surfaces," *Advanced Materials*, vol. 29, no. 27, p. 1700496, 2017.

[26] M. Liu, J. Wu, and H. Cheng, "Effects of laser processing parameters on properties of laser-induced graphene by irradiating co2 laser on polyimide," *Science China Technological Sciences*, vol. 65, no. 1, pp. 41–52, 2022.

[27] J. de la Roche, I. López-Cifuentes, and A. Jaramillo-Botero, "Influence of lasing parameters on the morphology and electrical resistance of polyimide-based laser-induced graphene (lig)," *Carbon Letters*, vol. 33, no. 2, pp. 587–595, 2023.

[28] A. Behrent, C. Griesche, P. Sippel, and A. J. Baeumner, "Process-property correlations in laser-induced graphene electrodes for electrochemical sensing," *Microchimica Acta*, vol. 188, pp. 1–14, 2021.

[29] F. Wang, K. Wang, B. Zheng, X. Dong, X. Mei, J. Lv, W. Duan, and W. Wang, "Laser-induced graphene: preparation, functionalization and applications," *Materials technology*, vol. 33, no. 5, pp. 340–356, 2018.

[30] Z. Zhang, H. Zhu, W. Zhang, Z. Zhang, J. Lu, K. Xu, Y. Liu, and V. Saetang, "A review of laser-induced graphene: From experimental and theoretical fabrication processes to emerging applications," *Carbon*, p. 118356, 2023.

[31] A. Mostaccio and G. Marrocco, "Design, prototyping, and characterization of laser-induced graphene (lig) antennas on flexible substrates," *Antennas and Propagation Magazine*, 2024, accepted.

[32] D. Froumsia, E. D. Jean-François, A. Houwe, K. Kolyang *et al.*, "Miniaturization of dual bands fractal-based microstrip patch fractal antenna for x and ku bands applications," *The European Physical Journal Plus*, vol. 137, no. 6, p. 746, 2022.

[33] C. Pfeiffer, "Fundamental efficiency limits for small metallic antennas," *IEEE Transactions on Antennas and Propagation*, vol. 65, no. 4, pp. 1642–1650, 2017.

[34] L. X. Duy, Z. Peng, Y. Li, J. Zhang, Y. Ji, and J. M. Tour, "Laser-induced graphene fibers," *Carbon*, vol. 126, pp. 472–479, 2018.

[35] Y. Houeix, F. J. Romero, D. P. Morales, N. Rodriguez, and D. Kaddour, "Novel frequency selective surface made of laser-induced graphene," in *2023 IEEE 13th International Conference on RFID Technology and Applications (RFID-TA)*. IEEE, 2023, pp. 257–260.

[36] D.-W. Wang, M.-J. Yuan, J.-Y. Dai, and W.-S. Zhao, "Electrical modeling and characterization of graphene-based on-chip spiral inductors," *Micromachines*, vol. 13, no. 11, p. 1829, 2022.

[37] J. S. Gomez-Diaz, J. Perruisseau-Carrier, P. Sharma, and A. Ionescu, "Non-contact characterization of graphene surface impedance at micro and millimeter waves," *Journal of Applied Physics*, vol. 111, no. 11, 2012.

[38] F. Majeed, T. Fickenscher, M. Shahpari, and D. V. Thiel, "Measurement of surface conductivity of graphene at w-band," *Microwave and Optical Technology Letters*, vol. 61, no. 7, pp. 1747–1754, 2019.

[39] F. Smits, "Measurement of sheet resistivities with the four-point probe," *Bell System Technical Journal*, vol. 37, no. 3, pp. 711–718, 1958.

[40] A. Mostaccio, G. Antonelli, M. Bragaglia, E. Martinelli, and G. Marrocco, "Comparative evaluation of laser-induced graphene (lig) traces on polyimide under soft and hard stress for iot applications," *IEEE Journal on Flexible Electronics*, vol. 2, no. 3, pp. 256–264, 2023.

[41] L. Hao, J. Gallop, S. Goniszewski, O. Shaforost, N. Klein, and R. Yakimova, "Non-contact method for measurement of the microwave conductivity of graphene," *Applied Physics Letters*, vol. 103, no. 12, 2013.

[42] A.-H. Boughriet, C. Legrand, and A. Chapoton, "Noniterative stable transmission/reflection method for low-loss material complex permittivity determination," *IEEE Transactions on Microwave Theory and Techniques*, vol. 45, no. 1, pp. 52–57, 1997.

[43] J. M. Catala-Civera, A. J. Canos, F. L. Penaranda-Foix, and E. de los Reyes Davo, "Accurate determination of the complex permittivity of materials with transmission reflection measurements in partially filled rectangular waveguides," *IEEE Transactions on Microwave Theory and Techniques*, vol. 51, no. 1, pp. 16–24, 2003.

[44] X.-C. Wang, A. Díaz-Rubio, and S. A. Tretyakov, "An accurate method for measuring the sheet impedance of thin conductive films at microwave and millimeter-wave frequencies," *IEEE Transactions on Microwave Theory and Techniques*, vol. 65, no. 12, pp. 5009–5018, 2017.

[45] B. D. Abera, I. Ortiz-Gómez, B. Shkodra, F. J. Romero, G. Cantarella, L. Petti, A. Salinas-Castillo, P. Lugli, and A. Rivadeneyra, "Laser-induced graphene electrodes modified with a molecularly imprinted polymer for detection of tetracycline in milk and meat," *Sensors*, vol. 22, no. 1, p. 269, 2021.

[46] Y. Chyan, R. Ye, Y. Li, S. P. Singh, C. J. Arnusch, and J. M. Tour, "Laser-induced graphene by multiple lasing: toward electronics on cloth, paper, and food," *ACS nano*, vol. 12, no. 3, pp. 2176–2183, 2018.

[47] M. Abdulhafez, G. N. Tomaraei, and M. Bedewy, "Fluence-dependent morphological transitions in laser-induced graphene electrodes on polyimide substrates for flexible devices," *ACS Applied Nano Materials*, vol. 4, no. 3, pp. 2973–2986, 2021.

[48] Y. Wang, G. Wang, M. He, F. Liu, M. Han, T. Tang, and S. Luo, "Multifunctional laser-induced graphene papers with combined defocusing and grafting processes for patternable and continuously tunable wettability from superlyophilicity to superlyophobicity," *Small*, vol. 17, no. 42, p. 2103322, 2021.

[49] M. K. Yazdi, A. Manohar, A. Olejnik, A. Smułka, A. Kramek, M. Pierpaoli, M. R. Saeb, R. Bogdanowicz, and J. Ryl, "Elucidating charge transfer process and enhancing electrochemical performance of laser-induced graphene via surface engineering with sustainable hydrogel membranes: An electrochemist's perspective," *Talanta*, vol. 281, p. 126836, 2025.

[50] I. Childres, L. A. Jauregui, W. Park, H. Cao, Y. P. Chen *et al.*, "Raman spectroscopy of graphene and related materials," *New developments in photon and materials research*, vol. 1, pp. 1–20, 2013.

[51] A. Kaidarova and J. Kosel, "Physical sensors based on laser-induced graphene: A review," *IEEE Sensors Journal*, vol. 21, no. 11, pp. 12 426–12 443, 2020.
[52] J. L. Beckham, J. T. Li, M. G. Stanford, W. Chen, E. A. McHugh, P. A. Advincula, K. M. Wyss, Y. Chyan, W. L. Boldman, P. D. Rack *et al.*, "High-resolution laser-induced graphene from photoresist," *ACS nano*, vol. 15, no. 5, pp. 8976–8983, 2021.
[53] *Super ShieldTM Silver Conductive Spray Paint*.
[54] M. Dordanihaghighi, M. Arjmand, and M. H. Zarifi, "Microwave investigation of dmso-doped pedot: Pss patch resonators under varying relative humidity," *Advanced Materials Technologies*, p. 2400708, 2024.
[55] B. Marinho, M. Ghislandi, E. Tkalya, C. E. Koning, and G. de With, "Electrical conductivity of compacts of graphene, multi-wall carbon nanotubes, carbon black, and graphite powder," *Powder technology*, vol. 221, pp. 351–358, 2012.
[56] B. Li, Y. Mao, X. Mao, Y. Liu, X. Li, Y. Zhou, S. Wang, F. Yang, C. Gao, and L. Wang, "Enhancement of the electrical conductivity and thermoelectric performance of single-walled carbon nanotubes by the introduction of conjugated small molecules with cation groups," *ACS Applied Energy Materials*, vol. 3, no. 12, pp. 11 947–11 955, 2020.
[57] F. Bouzidi, H. Aubert, D. Bajon, and H. Baudrand, "Equivalent network representation of boundary conditions involving generalized trial quantities-application to lossy transmission lines with finite metallization thickness," *IEEE transactions on microwave theory and techniques*, vol. 45, no. 6, pp. 869–876, 1997.
[58] J. Y. Siddiqui, C. Saha, and Y. M. Antar, "Compact srr loaded uwb circular monopole antenna with frequency notch characteristics," *IEEE Transactions on Antennas and Propagation*, vol. 62, no. 8, pp. 4015–4020, 2014.
[59] Chemtronics, "Circuitworks conductive epoxy," https://www.chemtronics.com/circuitworks-conductive-epoxy-2, 2023.
[60] D. M. Pozar, *Microwave engineering: theory and techniques*. John wiley & sons, 2021.